PHYSICAL REVIEW MATERIALS **9**, L111202 (2025)

Letter

Optimization of the growth of Sb_2Te_3 by MBE using thermally cracked Sb

Craig S. Knox,[1,2] Ahmet Yagmur,[1] Joel J. Burton,[1] Zabeada Aslam,[3] Philippa M. Shepley,[1] John Harrington,[3]
Edmund H. Linfield,[2] Joshua R. Freeman,[2] and Satoshi Sasaki[1]
[1]*School of Physics and Astronomy, University of Leeds, Leeds LS2 9JT, United Kingdom*
[2]*School of Electronic and Electrical Engineering, University of Leeds, Leeds LS2 9JT, United Kingdom*
[3]*School of Chemical and Process Engineering, University of Leeds, Leeds LS2 9JT, United Kingdom*

(Received 28 February 2025; accepted 15 October 2025; published 19 November 2025)

We have performed a materials investigation into the properties of antimony telluride films, grown by molecular beam epitaxy (MBE) as the temperature of an antimony cracking zone was varied. Through x-ray diffraction, magnetotransport studies, and examination using transmission electron microscopy, we find that as the cracker temperature is increased, the formation of defects is suppressed, due to the higher surface mobilities of the smaller antimony molecular species. This work highlights the importance of using a cracker cell and its optimization for the growth of high quality MBE grown films of Sb_2Te_3.

DOI: 10.1103/69xs-pvg1

Introduction. Antimony telluride (Sb_2Te_3) has attracted considerable attention recently as a material system for its topologically insulating properties, principally as part of an alloy [such as $(Bi_xSb_{(1-x)})_2Te_3$]. Within such a topological insulator (TI), transport should be dominated by dispersionless, Dirac-like surface states, where 180° backscattering is forbidden by spin-momentum locking [1,2]. In particular, coupling between surfaces and other interesting states of matter, such as magnetic materials or superconductors, is of particular interest to fabricate a new generation of quantum devices (such as novel resistance standards or components within a quantum computer). Additionally, the two-dimensional (2D) nature of the Sb_2Te_3 crystal can lead to nonlinear optical properties which are useful for future optoelectronic devices [3–5].

In order to have precise control over these interfaces and the crystal structure of the as-deposited films, molecular beam epitaxy (MBE) has been adopted as the preferred technique for growing high quality films of Sb_2Te_3 and its alloys, not only for easily enabling the growth of heterostructures [6,7] but also for the high degree of control over the deposition conditions that can be achieved. This allows the growth of large, uniform, high quality material which can be readily fashioned into interesting devices. However, the quality of MBE grown films of Sb_2Te_3 are still not able to match the electrical properties of exfoliated flakes, motivating further optimizations to improve film quality.

A feature of MBE is that the growth is highly sensitive to the substrate conditions. This true even in the case of a material like Sb_2Te_3, which is formed of quintuple layers held together by van der Waals (vdW) forces. The interface between the substrate and the overlying film can become a nucleation site for defects and dislocations, which can propagate through the lattice [8,9]. While the topologically protected surface states should theoretically be robust against these defects, real topological materials often host topologically trivial, bulk carriers, the number and mobility of which can be modulated by these defects.

It is, therefore, a key challenge to verify the topological properties of the surface states, due to the bulk p-type doping in Sb_2Te_3 materials. The most conclusive evidence of topological properties comes from angle-resolved photoemission spectroscopy measurements, where the band structure, and the Dirac cone in particular, can be imaged directly. However, this can only probe filled states below the Fermi level, and hence has difficulty resolving the band structure of p-type materials [10]. Of relevance to applications, magnetotransport studies can reveal the topological character of surface states, but such measurements require samples with extremely high mobility, and thus low defect density. Additionally, topologically trivial residual bulk carriers can obscure topological effects [11,12]. As the electronic properties of a material determine its permittivity, optoelectronic devices are also sensitive to these defects. This is alongside with any effects that reduce the crystalline order or the size of crystalline domains, which can hamper the nonlinear optical properties of these materials [4,13]. As such, improving the quality of Sb_2Te_3 is essential to develop topologically insulating and optoelectronic devices from Sb_2Te_3, and to improve the quality of TIs based on it, such as $(Bi_xSb_{(1-x)})_2Te_3$, where the bulk p-type doping is suppressed by alloying the Sb_2Te_3 with n-type Bi_2Te_3. In addition, the interface between Sb_2Te_3 and the underlying substrate is itself an interesting topic of study, as conventional Rashba spin split surface states have been identified on the surfaces of thin films [14,15]. In order to probe these states, or utilize them in conventional spintronic devices, sharp, defect free interfaces are required.

In order to suppress the formation of defects at the substrate-film interface, the mobility of adatoms on the growth surface is a key control parameter within MBE. However, many Sb_2Te_3 films and their alloys are grown with the antimony evaporated from a conventional single-filament effusion cell [16–18]. Within such effusion cells, antimony evaporates in a molecular cluster, Sb_4, which has a low surface mobility. Within more conventional semiconductors such as GaSb, this low mobility has been linked to the formation of antisite defects and vacancies. If this was to occur within Sb_2Te_3, these defects would act as dopants and result in the topological surface states being obscured. To remedy this, the molecular cluster of antimony can be thermally broken apart in an effusion cell equipped with a cracker zone, with the resulting species (Sb_2, Sb_1) possessing superior surface mobility [19,20]. This is expected to be particularly important in the growth of Sb_2Te_3 as the growth will be limited by the sticking coefficient of the antimony species.

Here we report a study of four Sb_2Te_3 samples grown using MBE where only the temperature of the Sb cracking zone is varied. We find that there is a substantial improvement in the crystalline quality and electrical mobility when the Sb is cracked down to its atomic form. Transmission electron microscopy (TEM) and selected area electron diffraction (SAED) images show that the films grown with a higher cracker temperature have a lower number of in-plane defects and twinning boundaries. This presents a mechanism by which the properties of Sb_2Te_3 and $(Bi_xSb_{(1-x)})_2Te_3$ systems can be optimized.

Sample preparation and experimental details. Sb_2Te_3 samples were grown on {0001} oriented Al_2O_3 substrates by codeposition of evaporated antimony and tellurium from valved cracker sources in a solid-source MBE system, with a base pressure of $\approx 1 \times 10^{-10}$ mbar. The samples were grown in a two-step process. First, a ∼5-nm-thick nucleation layer was deposited at 170 °C. The sample temperature was then raised to the growth temperature of 225 °C, where the rest of the film was grown. Without the nucleation step, adhesion to the substrate was poor, and a uniform film could not be produced. All temperatures were measured with a thermocouple attached to the sample manipulator.

Samples were grown under chalcogenide rich conditions, where the tellurium flux was set to be 20 times that of the antimony flux, as measured by a beam flux monitor close to the sample manipulator. This tellurium-rich environment is essential in order to minimize the formation of chalcogenide vacancies [8]; obtain the correct phase of TI [21]; and ensure that the growth rate is determined solely by the antimony flux [22]. This Sb/Te ratio is maintained by choosing an Sb flux, and then tuning the temperature of the Te reservoir, and the position of the needle valve on the Te cell, to achieve the desired ratio. The temperature of the tellurium cracker zone was held 200 °C above the tellurium reservoir, resulting in cracker zone temperatures between 550 and 580 °C. Different samples were then produced by tuning the temperature of the cracker zone on the antimony cell between 700 and 900 °C, while maintaining a constant antimony flux. Finally, the samples were cooled under a tellurium flux at 3 °C/min in order to maintain the surface quality.

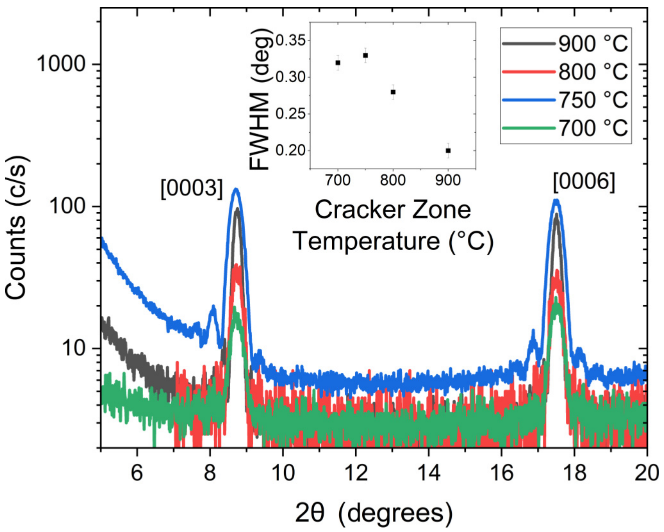

FIG. 1. XRD characterization of the Sb_2Te_3 samples. All samples show the expected $R\bar{3}M$ crystal structure, with the c axis parallel to the growth direction. Known diffraction peaks are labeled by the relevant Miller indices. The inset shows the variation of the FWHM of the [0006] peak as a function of Sb cracker temperature.

The crystallographic properties of Sb_2Te_3 samples were analyzed by x-ray diffraction (XRD), using Cu K_α radiation, before being diced for fabrication. The samples were patterned into Hall bars using optical lithography and chemical wet etching, before Cr/Au ohmic contacts were deposited by thermal evaporation. Transverse and Hall resistances were subsequently recorded by standard lock-in techniques with a source-drain bias current of 1 μA at a frequency of 119.77 Hz in a continuous flow He cryostat with a base temperature of 1.6 K and an 8 T superconducting magnet. TEM analysis was carried out using the FEI Titan Themis Cubed, operated at 300 kV. The selected-area electron diffraction patterns were collected using a SAED aperture of projected size ≈180 nm. Images were collected on the Gatan OneView 16 Megapixel CMOS digital camera.

Results. The $(\omega - 2\theta)$ XRD scans of the Sb_2Te_3 samples are shown in Fig. 1. All samples show well ordered $\{0003l\}$ peaks, indicating that the c axis of the material is ordered parallel to the growth direction with a lattice parameter of 3.03 ± 0.02 nm, being consistent with previously published studies on this material [23,24]. All wafers show Pendellosung fringes around the [0003] peak, indicating strong ordering along the c axis. Analysis of these fringes reveal the thickness of all films to be 21 ± 3 nm. When we consider the full width at half maximum (FWHM) of the [0006] peak, as shown in the inset of Fig. 1, we note that as the cracker temperature is increased, the FWHM of the XRD peaks decreases. This implies that as the Sb is broken down into lighter molecular species, the film becomes more ordered.

This degree of ordering was then probed through measuring the electronic properties. All samples showed sheet resistances that decrease with decreasing temperature, as depicted in Fig. 2(a). Such behavior is indicative of a highly-doped semiconductor, where the transport is limited by the phonon scattering rate at high temperature, rather than the

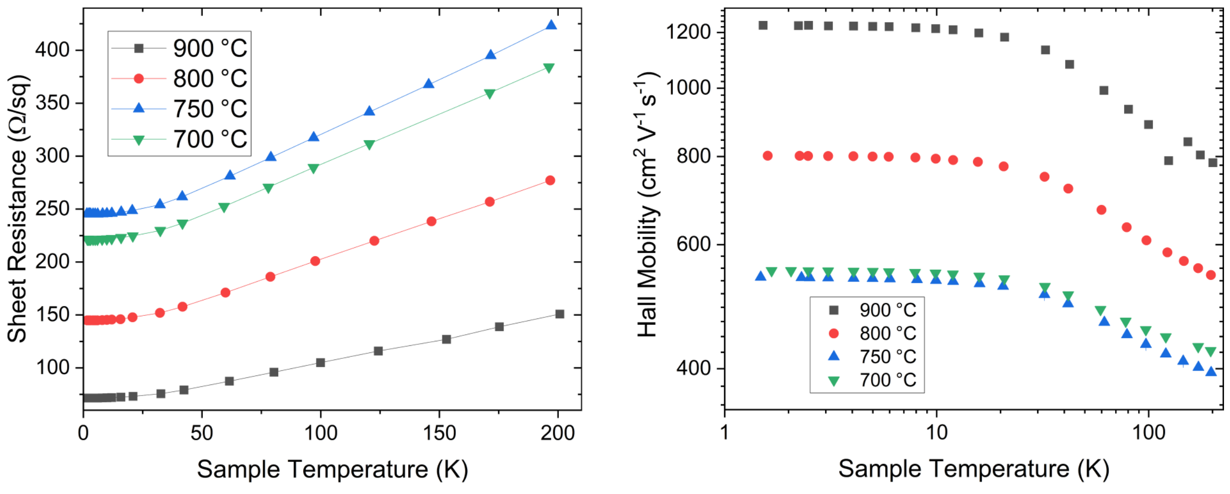

(a)

(b)

FIG. 2. Temperature-dependent transport properties of the Sb_2Te_3 samples. (a) shows the variation in sheet resistance as a function of temperature. (b) shows the effect of temperature on the Hall mobility. Two regimes are apparent for all samples, a low temperature regime $T < 20\,\text{K}$ where the mobility is temperature independent, and a high temperature regime ($T > 50\,\text{K}$) where the scattering is phonon-mediated.

carrier density. The temperature dependence of the Hall mobility, as shown in Fig. 2(b), also shows scattering typical of a highly doped semiconductor, with the mobility separated into two regimes; a low temperature regime ($T < 20\,\text{K}$), where temperature-independent impurity scattering dominates, and a high temperature regime $T > 50\,\text{K}$ in which phonon scattering leads to a decrease in mobility with increasing temperature. Across all temperature regimes, the transport through the Sb_2Te_3 films is hole-dominated. This is consistent with transport being dominated by the topologically trivial bulk carriers. Previous studies of the band-structure of Sb_2Te_3 shows that the Fermi energy is pinned within the bulk valence bands [10]. If the surface states were to dominate the transport we would expect to observe the freeze-out of those bulk carriers at high temperatures, leading to a regime where resistance increases with decreasing temperature, followed by a re-emergence of a regime where the resistance decreases with decreasing temperature as the transport becomes limited by the scattering within the surface states [25,26]. As we do not observe this crossover, we conclude that the surface states make a relatively minor contribution to the overall transport within our samples.

Two additional points emerge from the analysis of this transport data; firstly, the higher the cracker temperature, the lower the defect density within the Sb_2Te_3 crystal, as shown by the higher low temperature mobility. Secondly, the phonon-dominated scattering above 50 K results in the mobility showing a power law dependence with temperature, $\mu \propto T^a$. Interestingly, the samples with cracker temperatures of 900 °C and 800 °C both show a power law dependence of $a = -0.17 \pm 0.02$, whereas the 750 °C and 700 °C samples show power law dependences of $a = -0.13 \pm 0.01$ and $a = -0.10 \pm 0.01$, respectively. As none of these exponents correspond to commonly observed scattering mechanisms [27,28] multiple scattering mechanisms must be present. Fitting the temperature dependence of the sheet resistance to the Bloch Grüneisen formula [29] reveals a similar Debye temperature of $185 \pm 5\,\text{K}$ for all samples. This is similar to the bulk Debye temperature of 160 K [30,31], and implies that the behavior of the phonons within these Sb_2Te_3 samples is similar. The change in the temperature scaling of the mobility is thus likely to be due to an increased defect density.

All measured samples show weak antilocalization (WAL) at temperatures below 10 K, as shown in the inset of Fig. 3. This behavior can be described by the Bergmann

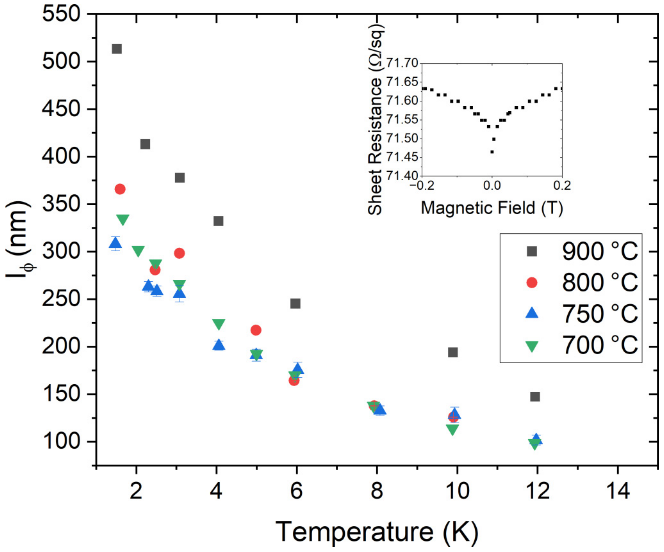

FIG. 3. Temperature variation of the phase-breaking length l_ϕ for the Sb_2Te_3 samples. In all samples l_ϕ has a power-law dependence consistent with electron-electron scattering within a 2D Fermi liquid (i.e $l_\phi \propto T^{-0.5}$). Inset: The WAL response at 1.5 K for the sample grown with a 900 °C cracker temperature.

model (assuming no magnetic scattering) [32]:

$$\Delta\sigma_{xx}(B) = \frac{-e^2}{2\pi^2 h}\left[\left(\Psi\left(\frac{1}{2}+\frac{B_a}{B}\right)\right) - \frac{3}{2}\left(\Psi\left(\frac{1}{2}+\frac{B_b}{B}\right)\right) + \left(\Psi\left(\frac{1}{2}+\frac{1}{2}\frac{B_c}{B}\right)\right)\right]. \tag{1}$$

Here, $B_a = B_e + B_{\text{so}}$, $B_b = B_\phi + \frac{4}{3}B_{\text{so}}$, $B_c = B_\phi$, Ψ is the digamma function, and $\Delta\sigma_{xx}$ is the change in conductivity arising from WAL compared to a classical system. B_e, B_ϕ, and B_{so} are the characteristic fields associated with elastic, inelastic and spin-orbit scattering, respectively, and can be related to their scattering times by $B_x\tau_x = \frac{\hbar}{4eD}$, where τ_x is the relevant scattering time, and D is the electronic diffusion coefficient for the material being studied. This scattering time can then be converted into a scattering length; $l_x = (D\tau_x)^{\frac{1}{2}}$. It should be noted that l_e can be estimated from $\sigma_{xx}(T = T_{\text{min}}, B = 0)$. As we have shown that the dominant scattering mechanism is temperature-independent impurity scattering within this temperature range, l_e and thus B_e can be treated as constant with respect to temperature. As such, the number of fitting parameters can be reduced to two (B_ϕ and B_{so}). As expected, all samples show a l_{so} that is also independent of temperature, with $l_{\text{so}} = 5 \pm 3$ nm, 20.7 ± 0.1 nm, 12 ± 1 nm, and 33 ± 1 nm for the samples grown at cracker temperatures of 900 °C, 800 °C, 750 °C, and 700 °C, respectively.

All samples show l_ϕ (i.e., the scattering length corresponding to inelastic scattering) that scales with a power law of $T^{-0.55\pm0.05}$ (as shown in Fig. 3), consistent with the main phase-breaking mechanism being small energy electron-electron scattering within a 2D Fermi liquid (i.e., $l_\phi \propto T^{-0.5}$) [33]. Similar responses have been observed in a wide variety of TI systems [34,35], regardless of the level of coupling between bulk and surface states [34] or whether the transport is dominated by bulk or surface conduction [35]. This further reinforces the fact that the main difference between the samples is the increased impurity concentration from samples grown with a lower cracker temperature. Contributions from increased phonon scattering or impurity states would result in a T^{-1} dependence [33,36,37], whereas a $T^{-0.25}$ dependence could be indicative of charge puddles within the surface states [36].

In order to understand the microscopic origin of the disorder in the Sb_2Te_3 samples, lamellae were extracted from the as-grown film by focused ion beam milling and measured using TEM. High angle annular dark field (HAADF) images reveal the quintuple layer structure of the Sb_2Te_3 films, as shown in the inset of Fig. 4(a), confirming the $\{0003l\}$ ordering seen in the XRD. The films were then examined using SAED (Fig. 4). It is important to note that the images show contributions from all three layers within the stack; the sapphire substrate, the Sb_2Te_3 and the amorphous layer used to encapsulate the lamellae. Images taken from only the sapphire and only from the amorphous layer are shown in the insets of Figs. 4(c) and 4(d), respectively.

This analysis reveals two things; first, there is a significant lattice mismatch between the underlying sapphire and the Sb_2Te_3 film (as shown by the differing periodicities in the SAED images), which is expected of a VdW material [38]. Secondly, while all the patterns show a similar c axis periodicity of 1.0 ± 0.1 nm (the thickness of a single Sb_2Te_3 quintuple layer [39]), the diffraction spots are significantly more diffuse for the more disordered samples, particularly away from the central diffraction spots along the c axis.

Figure 4(d) shows a possible reason for this broadening of the diffraction spots, with doubled Sb_2Te_3 spots (one of which is highlighted with a red circle) becoming visible in the diffraction pattern, indicative of the formation of twinning domains within the crystal structure. A diffracted electron incident on a twinning boundary may be diffracted a second time, resulting in a displacement of the electron and the apparent doubling of diffraction spots within a SAED image [40]. Twinning domains have been observed in other TI films, usually nucleating around dislocation defects at the substrate-TI interface [41,42]. This implies that the defects responsible for the reduced quality of the lower cracker temperature samples arise from an increased density of dislocation defects, resulting in additional scattering sites forming at twin-domain boundaries. These dislocations are likely to be a result of the lower surface mobility of the larger Sb clusters [19,20]. If a cluster of Sb_4 is incident on the surface during growth, one or more atoms in the cluster may not bond to a lattice site, forming a dislocation. If Sb is cracked into its atomic form, this is much less likely to occur, resulting in the suppression of such defects. It is important to note that this is not the case with the Te adatoms, as the substrate temperature is held high enough to re-evaporate any Te that is not well integrated into the lattice [22].

Conclusions. We have grown using MBE a series of Sb_2Te_3 samples, where both adatoms were evaporated through valved cracker cells. Through examining the material properties of these materials using XRD, TEM, and selected area electron diffraction, we find that the crystalline order of these materials is substantially enhanced by cracking the antimony down into an elemental form (using a cracker zone temperature of 900 °C), and this enhances the electron mobility and spin orbit coupling strength. This is due to the higher mobility of the antimony adatoms on the growth surface, leading to the suppression of dislocation defects caused by improper integration of Sb clusters into the crystal lattice. As Sb_2Te_3 forms the basis for the bulk-insulating $(Bi_xSb_{(1-x)})_2Te_3$ ternary system, these results will help facilitate growth of higher quality material for research into spintronics, Majorana fermions and resistance standards utilizing the Quantum Anomalous Hall effect. Additionally the improved crystallinity of these films will be important to developing optoelectronic devices based on this 2D material.

Acknowledgments. The authors gratefully acknowledge the support of the LEMAS facility at the University of Leeds for their assistance with the Transmission Electron microscopy. The authors also gratefully acknowledge T. Moorsom for preliminary TEM measurements, and B. Hickey for fruitful discussions on the WAL analysis. This work was supported financially by the United Kingdom Research and Innovation councils through the grant Nanoscale Advanced Materials Engineering, Grant No. EP/V001914/1, as well as by the European Union through the project EXTREME-IR (EU Project No. 964735). The samples were grown in the Royce Deposi-

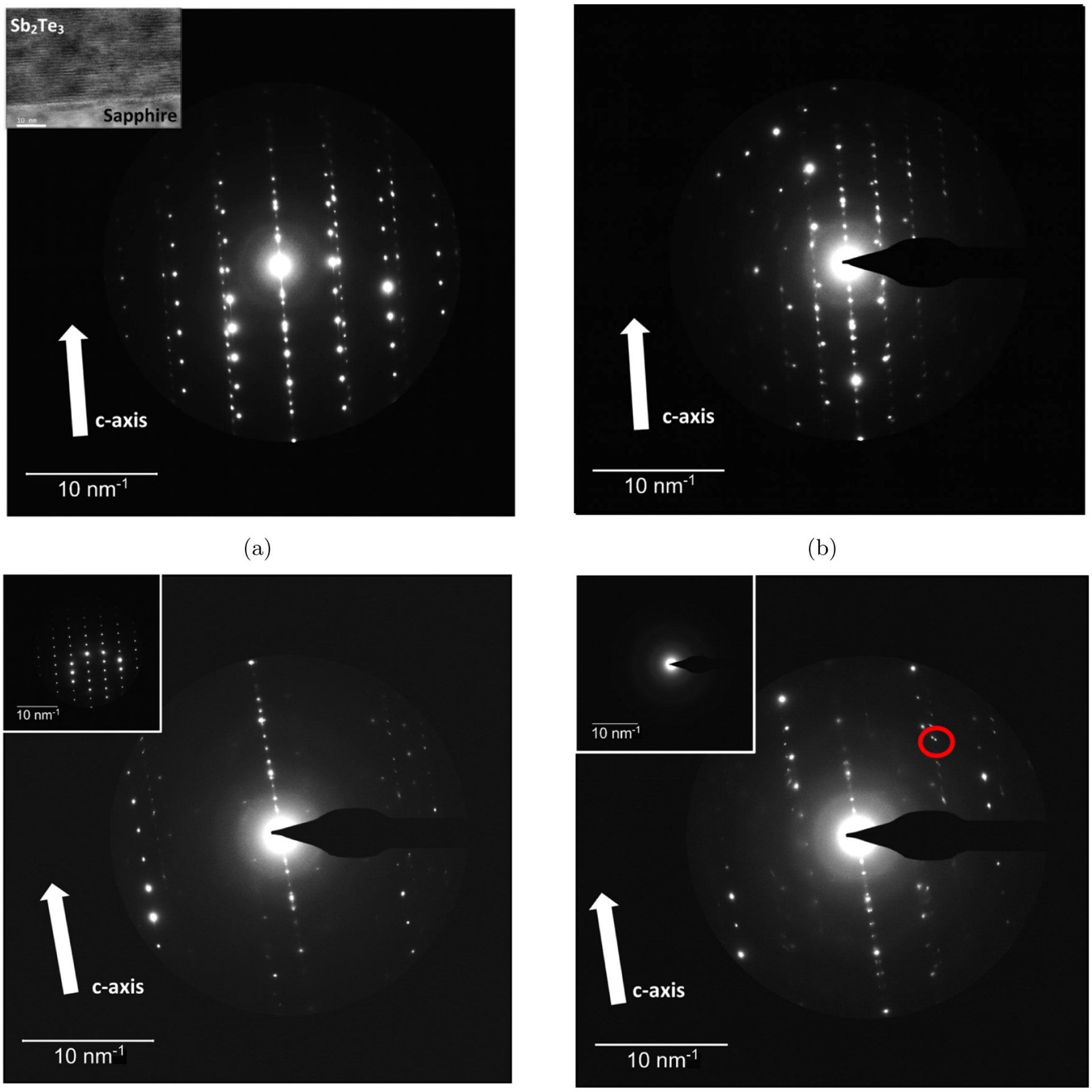

(a) (b)

(c) (d)

FIG. 4. SAED images of the Sb_2Te_3 samples grown with cracker zone temperature of 900 °C (a), 800 °C (b), 750 °C (c), and 700 °C (d). In all images there are two sets of repeating spots: the bright spots from the sapphire substrate, and the weaker spots from the Sb_2Te_3 film. The inset of (a) shows a HAADF image of the Sb_2Te_3 film, the inset of (c) shows the diffraction pattern from only the sapphire substrate, and the inset of (d) shows the diffraction pattern from only the amorphous layer used to encapsulate the Sb_2Te_3 film for FIB milling. All inset images were taken from the wafer grown at a cracker temperature of 900 °C. (b) and (d) show doubled diffraction spots arising from a twinning boundary. One such doubled diffraction spot is highlighted in (d) with a red circle.

tion system at the University of Leeds, which is supported by the Henry Royce Institute, United Kingdom, through Grants No. EP/P022464/1 and No. EP/R00661X/1.

Data availability. The data that support the findings of this article are openly available [43], embargo periods may apply.

---

[1] C. L. Kane and E. J. Mele, Quantum spin Hall effect in graphene, Phys. Rev. Lett. **95**, 226801 (2005).

[2] A. A. Taskin and Y. Ando, Berry phase of nonideal Dirac fermions in topological insulators, Phys. Rev. B **84**, 035301 (2011).

[3] C. Liu, L. Cheng, Y. Yuan, J. Su, X. Zhang, X. Li, H. Zhao, H. Zhang, Y. Zheng, and J. Li, Contrastive investigation on linear optical properties and nonlinear absorption behaviors between Sb_2Se_3 and Sb_2Te_3 thin films, Mater. Res. Express **6**, 086446 (2019).

[4] C. Moisset, R. N. Verrone, A. Bourgade, G. T. Zeweldi, M. Minissale, L. Gallais, C. Perrin-Pellegrino, H. Akhouayri, J. Lumeau, J. Y. Natoli, and K. Iliopoulos, Giant ultrafast optical nonlinearities of annealed Sb_2Te_3 layers, Nanoscale Adv. **2**, 1427 (2020).

[5] V. Bragaglia, M. Ramsteiner, D. Schick, J. E. Boschker, R. Mitzner, R. Calarco, and K. Holldack, Phonon anharmonicities and ultrafast dynamics in epitaxial Sb_2Te_3, Sci. Rep. **10**, 12962 (2020).

[6] X. Liu, D. Wu, L. Liao, P. Chen, Y. Zhang, F. Xue, Q. Yao, C. Song, K. L. Wang, and X. Kou, Temperature dependence of spin–orbit torque-driven magnetization switching in *in situ* grown Bi_2Te_3/MnTe heterostructures, Appl. Phys. Lett. **118**, 112406 (2021).

[7] R. van Haren and D. Lederman, Suppressed weak antilocalization in topological insulator–antiferromagnetic insulator $(BiSb)_2Te_3$-MnF_2 thin film bilayers, Phys. Rev. B **110**, 205409 (2024).

[8] N. Bansal, Y. S. Kim, E. Edrey, M. Brahlek, Y. Horibe, K. Iida, M. Tanimura, G. H. Li, T. Feng, H. D. Lee, T. Gustafsson, E. Andrei, and S. Oh, Epitaxial growth of topological insulator Bi_2Se_3 film on Si(111) with atomically sharp interface, Thin Solid Films **520**, 224 (2011).

[9] Z. Wang and S. Law, Optimization of the growth of the van der Waals materials Bi_2Se_3 and $(Bi_{0.5}In_{0.5})_2Se_3$ by molecular beam epitaxy, Cryst. Growth Des. **21**, 6752 (2021).

[10] L. Locatelli, A. Kumar, P. Tsipas, A. Dimoulas, E. Longo, and R. Mantovan, Magnetotransport and ARPES studies of the topological insulators Sb_2Te_3 and Bi_2Te_3 grown by MOCVD on large-area Si substrates, Sci. Rep. **12**, 3891 (2022).

[11] S. M. Huang, P. C. Wang, H. L. Jian, and M. M. Chou, The magnetic susceptibility bifurcation in the Ni-doped Sb_2Te_3 topological insulator with antiferromagnetic order accompanied by weak ferromagnetic alignment, Nanoscale Res. Lett. **16**, 180 (2021).

[12] Y. C. Huang, P. C. Lee, C. H. Chien, F. Y. Chiu, Y. Y. Chen, and S. R. Harutyunyan, Magnetotransport properties of Sb_2Te_3 nanoflake, Phys. B: Condens. Matter **452**, 108 (2014).

[13] A. V. Uklein, V. V. Multian, G. M. Kuz'micheva, R. P. Linnik, V. V. Lisnyak, A. I. Popov, and V. Y. Gayvoronsky, Nonlinear optical response of bulk ZnO crystals with different content of intrinsic defects, Opt. Mater. **84**, 738 (2018).

[14] C. Pauly, G. Bihlmayer, M. Liebmann, M. Grob, A. Georgi, D. Subramaniam, M. R. Scholz, J. Sánchez-Barriga, A. Varykhalov, S. Blügel, O. Rader, and M. Morgenstern, Probing two topological surface bands of Sb_2Te_3 by spin-polarized photoemission spectroscopy, Phys. Rev. B **86**, 235106 (2012).

[15] L. Plucinski, A. Herdt, S. Fahrendorf, G. Bihlmayer, G. Mussler, S. Döring, J. Kampmeier, F. Matthes, D. E. Bürgler, D. Grützmacher, S. Blügel, and C. M. Schneider, Electronic structure, surface morphology, and topologically protected surface states of Sb_2Te_3 thin films grown on Si(111), J. Appl. Phys. **113**, 053706 (2013).

[16] G. Behner, A. R. Jalil, D. Heffels, J. Kölzer, K. Moors, J. Mertens, E. Zimmermann, G. Mussler, P. Schüffelgen, H. Lüth, D. Grützmacher, and T. Schäpers, Aharonov-Bohm interference and phase-coherent surface-state transport in topological insulator rings, Nano Lett. **23**, 6347 (2023).

[17] K. S. Wickramasinghe, C. Forrester, and M. C. Tamargo, Molecular beam epitaxy of twin-free Bi_2Se_3 and Sb_2Te_3 on In_2Se_3/InP(111)B virtual substrates, Crystals **13**, 677 (2023).

[18] M. Lanius, J. Kampmeier, S. Kölling, G. Mussler, P. M. Koenraad, and D. Grützmacher, Topography and structure of ultrathin topological insulator Sb_2Te_3 films on Si(111) grown by means of molecular beam epitaxy, J. Cryst. Growth **453**, 158 (2016).

[19] Y. Rouillard, B. Lambert, Y. Toudic, M. Baudet, and M. Gauneau, On the use of dimeric antimony in molecular beam epitaxy, J. Cryst. Growth **156**, 30 (1995).

[20] Q. Xie, J. E. V. Nostrand, R. L. Jones, J. Sizelove, and D. C. Look, Electrical and optical properties of undoped GaSb grown by molecular beam epitaxy using cracked Sb_1 and Sb_2, J. Cryst. Growth **207**, 255 (1999).

[21] A. Fülöp, Y. Song, S. Charpentier, P. Shi, M. Ekström, L. Galletti, R. Arpaia, T. Bauch, F. Lombardi, and S. Wang, Phase transition of bismuth telluride thin films grown by MBE, Appl. Phys. Express **7**, 045503 (2014).

[22] S. Schreyeck, K. Brunner, A. Kirchner, U. Bass, S. Grauer, C. Schumacher, C. Gould, G. Karczewski, J. Geurts, and L. W. Molenkamp, Kinetic limitation of chemical ordering in $Bi_2Te_{3-x}Se_x$ layers grown by molecular beam epitaxy, J. Phys.: Condens. Matter **28**, 145002 (2016).

[23] M. Rimoldi, R. Cecchini, C. Wiemer, A. Lamperti, E. Longo, L. Nasi, L. Lazzarini, R. Mantovan, and M. Longo, Epitaxial and large area Sb_2Te_3 thin films on silicon by mocvd, RSC Adv. **10**, 19936 (2020).

[24] J. L. Lensch-Falk, D. Banga, P. E. Hopkins, D. B. Robinson, V. Stavila, P. A. Sharma, and D. L. Medlin, Electrodeposition and characterization of nano-crystalline antimony telluride thin films, Thin Solid Films **520**, 6109 (2012).

[25] F. Yang, A. A. Taskin, S. Sasaki, K. Segawa, Y. Ohno, K. Matsumoto, and Y. Ando, Top gating of epitaxial $(Bi_{1-x}Sb_x)_2Te_3$ topological insulator thin films, Appl. Phys. Lett. **104**, 161614 (2014).

[26] S. Shimizu, R. Yoshimi, T. Hatano, K. S. Takahashi, A. Tsukazaki, M. Kawasaki, Y. Iwasa, and Y. Tokura, Gate control of surface transport in MBE-grown topological insulator $(Bi_{(1-x)}Sb_x)_2Te_3$ thin films, Phys. Rev. B **86**, 045319 (2012).

[27] L. R. Testardi, J. N. Bierly, and F. J. Donahoe, Transport properties of p-type Bi_2Te_3-Sb_2Te_3 alloys in the temperature range 80–370°K, J. Phys. Chem. Solids **23**, 1209 (1962).

[28] D. Pinisetty and R. V. Devireddy, Thermal conductivity of semiconductor (bismuth–telluride)–semimetal (antimony) superlattice nanostructures, Acta Mater. **58**, 570 (2010).

[29] D. G. Westlake and L. C. Alfred, Determination of the debye characteristic temperature of vanadium from the Bloch-Grüneisen relation, J. Phys. Chem. Solids **29**, 1931 (1968).

[30] D. Zheng, S. Tanaka, K. Miyazaki, and M. Takashiri, Evaluation of specific heat, sound velocity and lattice thermal conductivity of strained nanocrystalline bismuth antimony telluride thin films, J. Electron. Mater. **44**, 1679 (2015).

[31] L. W. da Silva and M. Kaviany, Micro-thermoelectric cooler: Interfacial effects on thermal and electrical transport, Int. J. Heat Mass Transf. **47**, 2417 (2004).

[32] G. Bergmann, Weak localization in thin films: A time-of-flight experiment with conduction electrons, Phys. Rep. **107**, 1 (1984).

[33] G. Dumpich and A. Carl, Anomalous temperature dependence of the phase-coherence length for inhomogeneous gold films, Phys. Rev. B **43**, 12074 (1991).

[34] X. Li, M. Meng, S. Huang, C. Tan, C. Zhang, H. Peng, and H. Q. Xu, Surface-bulk coupling in a Bi_2Te_3 nanoplate grown by van der Waals epitaxy, Nanoscale **14**, 2586 (2022).

[35] R. K. Gopal, S. Singh, A. Mandal, J. Sarkar, and C. Mitra, Topological delocalization and tuning of surface channel separation in Bi_2Se_2Te topological insulator thin films, Sci. Rep. **7**, 4924 (2017).

[36] S. Singh, R. K. Gopal, J. Sarkar, S. Roy, and C. Mitra, Evidence of charged puddles and induced dephasing in topological insulator thin films, AIP Conf. Proc. **1953**, 50040 (2018).

[37] M. Kaveh and N. Wiser, Electron-electron scattering in conducting materials, Adv. Phys. **33**, 257 (1984).

[38] X. Zhang, Z. Zeng, C. Shen, Z. Zhang, Z. Wang, C. Lin, and Z. Hu, Investigation on the electrical transport properties of highly (00l)-textured Sb_2Te_3 films deposited by molecular beam epitaxy, J. Appl. Phys. **115**, 024307 (2014).

[39] F. Yang, A. A. Taskin, S. Sasaki, K. Segawa, Y. Ohno, K. Matsumoto, and Y. Ando, Dual-gated topological insulator thin-film device for efficient Fermi-level tuning, ACS Nano **9**, 4050 (2015).

[40] C. Cayron, Diffraction artefacts from twins and stacking faults, and the mirage of hexagonal, polytypes or other superstructures, Scr. Mater. **194**, 113629 (2021).

[41] A. Richardella, A. Kandala, J. S. Lee, and N. Samarth, Characterizing the structure of topological insulator thin films, APL Mater. **3**, 083303 (2015).

[42] Y. Tung, Y. F. Chiang, C. W. Chong, Z. X. Deng, Y. C. Chen, J. C. Huang, C. M. Cheng, T. W. Pi, K. D. Tsuei, Z. Li, and H. Qiu, Growth and characterization of molecular beam epitaxy-grown $Bi_2Te_{3-x}Se_x$ topological insulator alloys, J. Appl. Phys. **119**, 055303 (2016).

[43] C. S. Knox, A. Yagmur, J. J. Burton, Z. Aslam, P. M. Shepley, J. Harrington, E. H. Linfield, J. R. Freeman, and S. Sasaki, Dataset associated with optimization of the growth of Sb_2Te_3 by MBE using thermally cracked Sb, https://doi.org/10.5518/1654.